Simulation of Pressure-Driven Flows in Nanochannels Using Multiparticle Collision Dynamics†

Riyad Chetram Raghu and Jeremy Schofield*

Chemical Physics Theory Group, Department of Chemistry, University of Toronto, 80 Saint George Street, Ontario, Canada, M5S 3H6

Received: June 17, 2010; Revised Manuscript Received: September 14, 2010

A multiparticle collision dynamics algorithm is presented to simulate gas flow in nanoscopic channels with a square cross section. Special attention is given to the definition of inlet and outlet regions of the simulated system and the boundary conditions that are appropriate to describe flow through the nonequilibrium, open system. The boundary conditions are designed to use only physically relevant, readily measurable quantities as input, such as the pressure drop between ends of the channel, the mass flow rate, and the temperature at the input and output. Particular care is taken to minimize the propagation of entrance and exit artifacts due to the inlet and outlet regions by using Navier−Stokes solutions for the expected velocity profile in the first inlet cell. In addition, a collision operator is introduced to simulate an adiabatic diffusive boundary condition to facilitate the study of energy flow through the channel in the absence of thermalizing walls. The results of simulations over a range of conditions are compared to series solutions of the Navier−Stokes equation both with and without slip boundary conditions for isothermal compressible fluid flow in a square channel. The results of the particle-based simulation agree well with the slip boundary condition solution, although the assumption of isothermal flow begins to fail and deviations between the solution and simulation results begin to emerge under high pressure gradients.

Introduction

Nanofluidic and microfluidic systems in the gas and liquid phase are of great interest from both an industrial and a scientific standpoint. These systems have numerous applications, ranging from "lab on a chip"[1] models of a disposable chemical reactor that can perform diagnostic tests with a bare minimum of reagents to heat sinks within modern electronics. In addition, microfluidic systems can serve as an analogue of cellular and capillary transport in biological systems.

Theoretical modeling of channel flow provides valuable, but difficult to obtain, information on how flow properties are affected by features of the channel morphology. For large nonmesoscopic systems, the Navier−Stokes (NS) equation is frequently used to analyze flow profiles. The application of the NS equation can be justified from first principles for large, nonequilibrium, and steady-state systems by defining a probability density of local equilibrium form in which local thermodynamic variables are conjugate to slowly varying density fields of the number, momentum, and energy density.[2,3] When the length scale of spatial variations in the thermodynamic variables is large compared with microscopic correlation lengths, the NS equations for local equilibrium ensemble averages are obtained by gradient expansion of the equation of motion of the average density fields. Similar methods can be utilized for pair or higher-order correlation functions in steady-state systems by generalizing the notion of local equilibrium.[4] For many mesoscale systems, the requirement of slowly varying local densities underlying the NS equation breaks down because the system is too small to smoothly coarse grain the density fields, and local fluctuation effects become large and significant. For such systems, particle-based simulation methods are a more sensible approach.

The simulation of compressible channel flow through nanoscopic devices is complex. Mesoscale channel devices typically have large inlet and outlet reservoirs characterized by different thermodynamic states that lead to steady-state flow as the overall system equilibrates. As these reservoir regions involve many particles and are difficult to characterize, particularly near the channel, simulation studies usually attempt to model only the interior of the channel and replace the reservoirs with inlet and outlet regions that utilize boundary conditions to induce flow. From a simulation perspective, the large fluctuation effects in the nonequilibrium, open system complicate matters. Ideally, experimentally accessible thermodynamic variables of the reservoirs should be used to enforce boundary conditions that determine the flow field. However, this is seldom the case for particle-based simulations. Many simulation approaches for inducing flow in open, nonequilibrium systems are based on simple modifications to methods developed for closed equilibrium systems. Unfortunately, many of these methods for inducing flow have unphysical characteristics.

Even with the simplifications of replacing reservoirs with inlet and outlet regions, the number of particles flowing through the channel makes a full molecular dynamics study based on Newtonian dynamics prohibitively expensive. Fortunately, a complete molecular dynamics approach is not generally required to simulate most flow properties accurately in these devices. The minimal requirement for most quantities of interest is that the algorithm be capable of reproducing hydrodynamic behavior that is consistent with the Navier−Stokes equation. Thus, simulation methods must describe dynamics that locally conserves mass, energy, and momentum. Mesoscopic algorithms, such as direct simulation Monte Carlo (DSMC),[5] dissipative particle dynamics (DPD),[6] and multiparticle collision dynamics

† Part of the "Mark A. Ratner Festschrift".

* To whom correspondence should be addressed. E-mail: jmschofi@chem.utoronto.ca (J.S.).

10.1021/jp1055914
Published on Web 10/22/2010

MPC[7] (also known as stochastic rotation dynamics), can be used for this purpose.

Although channel flow has been studied using DSMC,[8−10] DPD,[11,12] and MPC,[13] the degree to which hydrodynamic behavior has been reproduced is highly dependent on the method used to induce flow. Several of these studies have utilized boundary conditions that are only appropriate for an incompressible fluid and often require a thermostat to remove excess kinetic energy that makes the study of energy transport difficult. For an incompressible fluid, channel flow is a pure shear flow, and methods, such as sliding-brick boundary conditions[14] or gravitational (forced) flows[11,13] with periodic inlet and outlet boundary conditions, can be used to generate the flow profile in a simulation. However, when the channel flow is compressible, there is an isentropic expansion of the fluid within the channel, leading to an elongational component to the flow that these methods are incapable of reproducing.

The simulation methods that are capable of describing a pressure-driven compressible flow in a channel can be divided into two classes, selective reflection[15] and source/sink methods.[8,11,15] The selective reflection method constructs a pressure gradient by modifying the periodic boundary conditions across the inlet and outlet. Particles are allowed to stream freely from the outlet to the inlet. Upon reaching the inlet boundary region, a stochastic approach in which particles are reflected with a probability p and allowed to pass with a probability $(1 - p)$ is implemented, and periodic boundary conditions are implemented at the outlet. Although this method can be used to create a pressure gradient and to establish a flow field and works well for systems with small (or even zero) gradients, the relationship between the reflection probability p and a desired pressure gradient is complex and not unique. More problematically, the temperature tends to drop unphysically in the absence of a thermostat, while the velocity increases systemically in the direction of flow over long simulations.

Source/sink methods induce flow by specifying the pressure, temperature, and transverse velocity at the inlet as well as the outlet pressure and transverse velocity. In this approach, the inlet and outlet act as a particle source or sink to maintain a specified boundary condition.[8] Although the method can recreate a flow field, large entrance and exit effects that persist well into the channel are evident when highly fluctuating local thermodynamic variables are used to define the boundary conditions, and instabilities in the form of shocks can develop. In addition, the gradient within the channel tends to be larger than specified, and a reversal of flow across the boundary can occur for small pressure gradients.

In this article, we present a particle-based simulation method using MPC[7] to model gas flow through a square channel. Modified source/sink boundary conditions are introduced that minimize the entrance effects typically associated with these conditions and allow for the simulation of small gradients. The algorithm requires that the outlet temperature be specified and utilizes the inlet velocity distribution obtained from an NS solution to stabilize flow profiles against large fluctuations. In this approach, particles are removed or inserted in the boundary cells based on time-averages of local state variables rather than their instantaneous values, and new particles are inserted in the first cell in the entrance region so that the average cell velocity corresponds to the mean velocity predicted from the NS equation without slip. Although this algorithm does not reproduce the expected pressure and number distributions within the boundary cells for an equilibrium system, the simulation method is stable and does maintain the correct equilibrium distributions within the channel without additional thermal control. This approach is consistent with the philosophy that the boundary cells are intended only as regions to model the reservoirs connected by the channel and are not themselves physically relevant.

The simulations presented here also utilize a collision model for particles interacting adiabatically with the wall of the channel that permits boundary region artifacts to be examined more carefully. Although Gaussian diffusion boundary conditions are commonly used and could be applied to simulate the interactions of solvent particles with the walls of the channel, these boundary conditions act as a thermostat and mask potential artifacts due to the particle insertion and removal mechanism utilized in the inlet and outlet regions. As an alternative, a collision operator is introduced to simulate the effect of adiabatic diffusive collisions. While a thermostatting particle−wall interaction is appropriate for the majority of micro- and nanofluidic devices, the adiabatic collision operator is useful for models of systems with thin walls with little thermalizing ability. Furthermore, a wall collision operator that allows for the fluid to cool due to its expansion is interesting from a thermodynamic perspective and for the modeling of macroscopic fluidic and aerodynamic devices.

To validate the simulation algorithm, the flow profiles of local thermodynamic variables resulting from simulation are compared to series solutions of the Navier−Stokes equation for isothermal flow with and without slip boundary conditions in the low Knudsen limit in which the mean free path is small relative to dimensions of the channel.

The next section outlines the simulation method, with a particular focus on boundary condition algorithms. The third section outlines the simulation conditions and parameters. The results of the equilibrium and flow simulations are presented in the fourth and fifth sections, respectively. The article terminates with a brief summary of the results.

MPC Algorithm

The MPC algorithm is a simplified version of a molecular dynamics method in which direct interactions between particles in the fluid are replaced by a random rotation of the momenta of the particles about local averages at discrete time intervals.[7,16] The simple nature of the collision process makes the MPC algorithm one of the most computationally efficient mesoscopic algorithms. Nonetheless, it allows for momentum transfer between fluid particles while maintaining conservation of mass, momentum, and energy. Because of the local conservation of global constants of the motion, an MPC system evolves to a state of maximum entropy, conserves phase space volume, and reproduces hydrodynamics in a bulk system consistent with the Navier−Stokes equation in the low rarefaction limit.[7]

In the MPC method, the dynamics consists of the concatenation of two types of evolution, the dynamical evolution of the position and momenta of all particles in the absence of fluid−fluid interactions, followed by the application of a collision operator that exchanges momentum among particles in a local region (for a review of this method, see ref 16). In the first step, all components of the system evolve for a predetermined period of time, τ_c, with the configuration of the system determined by solutions of the equations of motions in which there are no fluid−fluid interactions. The solution of the equation of motion frequently requires the implementation of numerical integration methods based on Hamiltonian splitting methods, such as the Verlet algorithm, over a short time interval, Δt, if the fluid particles interact with other bodies, such as solute particles. Typically, this time interval Δt is on the order of a

hundred times smaller than the collision time τ_c.[16] For pure fluid particle flow, the evolution of each of the fluid particles is independent of the others and can be solved exactly in many cases, even when the particles interact with an external wall potential.

After this evolution period, the particles undergo a rotation about the average momenta of the cell to simulate momentum exchange interactions between the particles of the fluid. First, the domain of the simulation is subdivided into cubic cells with a unit edge length, $l = 1$. The particles are displaced by a vector $\boldsymbol{\delta}$, constructed by drawing each of its Cartesian components from a uniform distribution on the interval $[-l/2, l/2]$ and assigned to cells based on their position. The momenta of the particles in the cells are rotated about the average momentum of the cell by an angle ϕ about a randomly chosen axis.

$$\boldsymbol{p}_i^* = \mathbf{M}_{\boldsymbol{k}}(\pm\phi)(\boldsymbol{p}_i - \bar{\boldsymbol{p}}) + \bar{\boldsymbol{p}}$$

where $\boldsymbol{p}_i^*$ is the postcollision momentum of particle i and $\bar{\mathbf{p}}$ is the average momentum of the particles in the cell. In the rotation or collision step, $\mathbf{M}_{\mathbf{k}}(\pm\phi)$ is the matrix for a rotation by an angle ϕ about an axis k. For each cell, the sign of ϕ is determined randomly, and in the implementation used here, k is selected to be one of the three coordinate axes of the system. After the momenta have been rotated, the position of the particles are displaced by $-\boldsymbol{\delta}$ to return them to their original position. This displacement step is meant to ensure that physical properties, such as local thermodynamic variables, are independent of global shifts in velocity and thereby restores Galilean invariance.[17]

The appropriate period for the rotation can be estimated from the mean collision time for a hard sphere fluid[18]

$$\tau_c = \frac{1}{2r^2(P_{in} + P_{out})}\sqrt{\frac{mk_BT}{\pi}} \qquad (1)$$

where r is the diameter of the hard sphere particle and P_{in} and P_{out} are the inlet and outlet pressures. When the rotation frequency is linked to a physical time, the data from the simulations take on a physical meaning, as this creates a physical correlation between position and momenta. In the simulations presented here, the inlet pressure was varied to study the effect of pressure gradients on flow properties in the channel. As a result, the collision times τ_c varied across simulations, and flow property data are presented in SI units, as opposed to dimensionless units based on intervals of τ_c.

Because fluid particles do not interact directly with one another, the equation of state of the fluid is ideal. However, it is possible to describe nonideal fluids by modifying the collision rule to account for excluded volume effects and obtain nonideal contributions to the pressure.[19]

As the channel is effectively an open system, a steady-state flow has to be induced by simulating the interface between the segment of channel that composes the system and the inlet, which is supplying the pressure head, and the outlet, which is supplying a back pressure. This is accomplished by treating the boundary cells as a particle source or particle sink as is required to specify the transverse velocity, pressure, and temperature at the inlet and to specify the transverse velocity and pressure at the outlet.[8] The complication in maintaining this boundary condition is an accurate determination of the mean velocity, which is necessary for the calculation of the pressure and temperature prior to making corrections. For the MPC simulations, a cell typically contains as few as 20 particles at any instant and, after a streaming step, no particles may have entered the system across the boundary. Given the magnitude of fluctuations of particle number and in dynamical variables representing quantities, such as the pressure, instantaneous local thermodynamic variables are difficult to use to establish stable boundary conditions. One alternative is to use a time average of the mean velocity from the cells one layer into the system to calculate the thermal velocity. Furthermore, it is insufficient to make corrections to only the layer of cells that interface directly with the system boundaries without creating instabilities in the flow field. Typically, multiple layers of cells require correction to ameliorate the interface between the boundary and the system.

For the simulations presented here, four layers of cells in the inlet and outlet comprise the boundary regions. For these additional layers of cells, a time average of the velocity in the cells is used for the corrections. The corrections themselves consist of either removing particles or adding particles with velocities drawn from a Maxwell−Boltzmann distribution with a desired temperature and mean velocity. If the measured pressure, P, is less than the specified pressure, $\bar{P}$, then particles with a velocity drawn from a Maxwell−Boltzmann distribution with temperature T and a mean velocity equal to the calculated mean velocity for the cell are added until the addition of particle $n + 1$ would increase the instantaneous difference of the pressure $|P_{n+1} - \bar{P}| > |P_n - \bar{P}|$, where P_n is the pressure with n particles. If $P > \bar{P}$, the particles are randomly selected to be destroyed until the destruction of particle $n - 1$ would lead to $|P_{n-1} - \bar{P}| > |P_n - \bar{P}|$. These corrections are made at time intervals Δt.

Although this procedure works well for systems with large pressure gradients, it produces large entrance and exit effects between the boundary region and the rest of the system. In particular, it produces a higher than specified inlet pressure and a lower than specified outlet pressure (see Figure 1), which makes it difficult to simulate systems with small pressure gradients. To remove these entrance effects, the basic algorithm is modified by using the NS solution for hydrodynamic flow in the square channel without slip boundary conditions (presented in the Appendix) for the mean velocity of the first layer of the inlet cells. The specification of the mean velocity in the first inlet cell stabilizes the system with respect to fluctuations in this quantity in the time average. To remove the memory of the previous Δt interval, the velocities of every particle in the first layer of the inlet and last layer of the outlet are redrawn prior to making a correction.

The other boundary condition that needs to be considered is the interaction between the fluid and the walls of the channel. This interaction is modeled by a collision operator. Typically, a Gaussian diffusion collision operator would be used to model a diffusive boundary condition;[20] however, this corresponds to an isothermal wall boundary condition and has a thermostatting effect on the fluid. In the absence of a thermalizing wall, the most commonly used particle−wall interaction consists of specular wall collisions, where the wall normal component of momentum is reversed. Such collisions ignore wall drag forces and might be viewed as full slip boundary conditions. Alternately, there are "bounce-back" or stick boundary conditions[13] where the particle momentum is completely reversed on collision.

To interpolate between the slip and stick limits of the wall interaction while conserving total energy, we introduce a generalization of the wall interactions that accounts for random irregularities in the wall surface. In this approach, the component of momentum normal to the surface of the wall at impact is

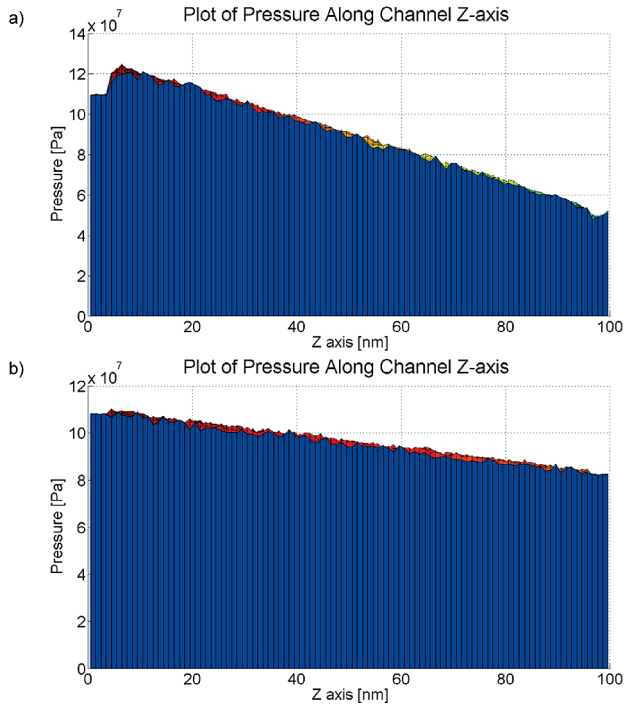

Figure 1. Inlet and outlet pressure deviations. In panels (a) and (b), source/sink boundary conditions are designed to establish a pressure gradient with an inlet ($z = 0$) pressure of 110.0 MPa and outlet pressure ($z = 100$ nm) of 82.3 MPa. Panel (b) uses the Navier−Stokes prediction of the inlet velocity to specify the mean velocity for the $z = 0.5$ nm layer of cells and redraws the velocities of every particle in the $z = 0.5$ nm and $z = 99.5$ nm layers of cells. In panel (a), only the time average of the local velocity for the $z = 0.5$ layer of cells is used to control particle insertion and deletion, and velocities are not redrawn.

reflected, and the remaining components of the momentum are rotated by a randomly selected angle, i.e.

$$\boldsymbol{p}^* = \mathbf{M}_{\hat{\mathbf{n}}}(\theta)\,\boldsymbol{p} - 2(\boldsymbol{p}\cdot\hat{\mathbf{n}})\hat{\mathbf{n}}$$

where $\boldsymbol{p}^*$ is the postcollision momentum, $\hat{\mathbf{n}}$ is a unit vector normal to the wall, and $\mathbf{M}_{\hat{\mathbf{n}}}(\theta)$ is the matrix for rotation by an angle θ about the $\hat{\mathbf{n}}$ axis. The rotation has the effect of maintaining the magnitude of the momentum vector, hence conserving energy. It also maintains the direction randomization effect of a particle−wall collision due to wall roughness and atomic motion. The wall interaction corresponds to an adiabatic boundary condition as there is no energy transfer between the particles and the wall. If θ is fixed at zero, this boundary condition corresponds to a full-slip specular collision. If θ is fixed at π, then the boundary condition corresponds to "bounce-back" or stick boundary conditions.

Gaussian diffusion boundary conditions draw the velocity from the following velocity density for the component of velocity normal to the wall, $v_\perp$

$$p(v_\perp) = \frac{mv_\perp}{k_B T}\exp\left(-\frac{mv_\perp^2}{2k_B T}\right)v_\perp$$

and redraw the tangential velocity components from a Maxwell−Boltzmann distribution.[20] For a fluid in thermal equilibrium, it is straightforward to show that the rotation boundary condition presented here produces the same velocity distribution.

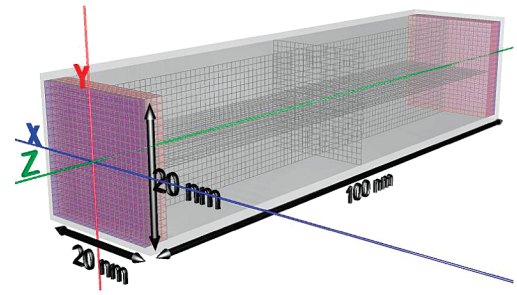

Figure 2. Model channel. This is a channel with a 20 nm × 20 nm square cross section and a length of 100 nm. The x and y axes are the wall normal axes of the system and are zero at the center of the channel; the z axis is the flow dimension and is zero at the channel inlet. The system is divided into 1 nm^3 cells. The first and last four layers of cells comprise the boundary condition regions of the system. The entrance layers are highlighted in purple, and the other boundary layers are highlighted in red.

In addition, the slip velocity can be modeled as[21]

$$v_{slip} = \alpha\lambda\left.\frac{dv_z(x,y)}{dx}\right|_{x=H/2} = \alpha\lambda\left.\frac{dv_z(x,y)}{dy}\right|_{y=H/2} \quad (2)$$

where α is the streamwise momentum accommodation and λ is the mean free path. This equation is often written in terms of the tangential momentum accommodation, σ_m, where $\alpha = (2 - \sigma_m)/\sigma_m$. This model is a first-order correction to nonequilibrium flow effects, initially developed by Maxwell.[22] If the collisions with the wall are diffusive, $\alpha = 1$.[23,24] As will be seen in the Flow Simulations section, the value of α found for these simulations is consistent with this value.

Simulation Conditions

A series of simulations were carried out to analyze the flow profiles induced by the boundary conditions for a range of pressure gradients, ranging from low flow rates, where the NS equation is expected to hold, to high rates, where significant deviations between the flow profiles of simulation and solution of the NS equation are anticipated, even with slip boundary conditions. The outlet pressure in the simulations was fixed at 82.3 MPa, which corresponds to an outlet density of 20 particles per cell, whereas the inlet pressure was increased to the drive the channel flow.

The simulations are performed in a model 20 nm × 20 nm × 100 nm channel ($H = 20$ nm, $L = 100$ nm) with 1 nm cubic cells ($l = 1$ nm) (see Figure 2). The choice of channel geometry was motivated by the fact that the cross section of nanofluidic and microfluidic devices tends to be square,[25] rectangular,[26] hexagonal,[27] rhombic, or trapezoidal.[28] The initial positions of fluid particles were drawn using uniform random variables, and the velocities were sampled from a Maxwell−Boltzmann distribution at the desired temperature with a mean velocity of zero. Simulation results for the velocity profile, flow rate, temperature profile, and density were recorded and compared to an analytical solution of the NS equation for square-channel flow presented in the Appendix.

The gas was modeled, with a diameter r of 0.083 nm and a mass of 39.943 amu. The equations of motion for the fluid particles were integrated with an integration time step, Δt, of 0.5 ps. The rotational period for each simulation was calculated using eq 1.

To obtain an entirely analytical form for the Navier−Stokes solution used both to calculate the streamwise velocity profile for the inlet boundary condition and to serve as a comparison to the results of the simulation, the viscosity, μ, was calculated from the MPC relation for the viscosity with rotation angle of 45°[29−31]

$$\mu = \frac{\rho k_B T \tau_c}{2}\left(\frac{3\rho^2 l^6 + 2\rho l^3 + 1 + \sqrt{2}(\rho^2 l^6 + 2^{-1/2} - 2)}{3\rho^2 l^6 - 2\rho l^3 - 1 - \sqrt{2}(\rho^2 l^6 + 2^{-1/2} - 2)}\right) + \frac{m\rho l^2(\rho l^3 - 1 + e^{-\rho l^3})}{18\tau_c \rho l^3} \quad (3)$$

As will be seen later, this expression for the viscosity matches the simulation values very well. The first 100 terms of the Navier−Stokes series solution for flow in a square channel derived in the Appendix were used to calculate the velocity profiles.

After simulation, the raw data were refined using a type one nonlinear regression to a nonspecific polynomial function. The Nelder−Mead simplex[32] was used as an extremization technique with a sum of least-squares norm and 90% confidence limits calculated by residual shuffling.[33] The initial coordinates for the simplex were generated using a genetic algorithm.[34] The genetic algorithm made use of mutation (20%), crossover (30%), interpolation (25%), and extrapolation (25%) operators, with a population size of 500 times the number of parameters plus 1 and 500 generations. Both global fits and local fits to the data were performed as the global fits lacked the precision to extract gradient data.

For the *global* fits of the simulation data, the velocity data were fit to the function

$$v_z(x,y,z) = \sum_{i=0}^{6}\alpha_i z^i\left(1 + \sum_{j=1}^{3}\beta_j(x^{2j} + y^{2j}) + \sum_{k=1}^{3}\sum_{l=k}^{3}\gamma_{kl}(x^{2k}y^{2l} + x^{2l}y^{2k})\right)$$

where α_i, β_j, and γ_{kl} are the adjustable parameters. Because of the symmetry of the flow profile about the central axis, the odd components of the polynomial could be eliminated. As the pressure and density data were axially homogeneous, they could be fitted to a sixth-degree polynomial that only varied along the length of the channel

$$\rho(z) = \sum_{i=0}^{6}\delta_i z^i$$

$$P(z) = \sum_{i=0}^{6}\varepsilon_i z^i$$

with adjustable parameters δ_i and ε_i.

The *local* data were fit to a cubic equation for one-dimensional data, and a modified tricubic equation was used in three dimensions. Furthermore, the contribution of residuals to the norm was scaled to $1/(1 + \omega)$, where ω is the distance from the point of interest to the data point. To facilitate the calculation, data points that were more than 10 nm from the point of interest in either the x, y, or z dimensions were omitted from the kernel. For the velocity data, the following equation was used

$$v_z(x,y,z) = \sum_{i=0}^{3}\alpha_i z^i\left(1 + \sum_{j=0}^{3}\sum_{k=0}^{\min(3,4-j)}\beta_{jk}x^j y^k\right)$$

where α_i and β_{jk} are adjustable parameters. For local values of the average velocity, density, and pressure, the following equation was used

$$\tau(z) = \sum_{i=0}^{3}\delta_i z^i$$

where $\tau(z)$ is the parameter being modeled and δ_i are the adjustable parameters.

Equilibrium Simulations

Equilibrium simulations were performed to validate the performance of the boundary condition algorithms relative to known conditions. The physical system under consideration consists of two large reservoirs connected by a nanoscale channel, with the entire system in thermal equilibrium. Although such a system is easily simulated with periodic boundary conditions, an equilibrium system poses significant challenges for sink/source boundary condition methods because small biases in thermodynamic variables within a boundary cell can lead to unphysical flow into or out of the boundary cells. In addition, the stabilizing effect of using a calculated mean velocity in the first boundary cell is not in evidence because no net flow exists in equilibrium. In contrast to the channel region, the reservoirs are sufficiently large that local thermodynamic variables can be easily defined over mesoscopically to macroscopically defined regions. On the other hand, dynamical variables that correspond to thermodynamic observables within the channel fluctuate significantly and have less physical meaning because a thermodynamic description is justified only for systems containing many particles. Nonetheless, the distributions of the dynamical variables for the pressure and number density for a cell can be easily calculated for a system in overall thermal equilibrium, provided one focuses on regions in the channel where boundary effects of the walls are minimal. For such a cell in the system, the local number density, n, should have a Poisson distribution in equilibrium

$$\rho_e(n) = \frac{1}{n!}\left(\frac{l^3\bar{P}}{k_B T}\right)^n \exp\left(\frac{-l^3\bar{P}}{k_B T}\right) \quad (4)$$

where $\bar{P}$ is the average pressure of the system. Similarly, the pressure in a cell should have a probability density for nonzero P given by

$$p_e(P) = \frac{1}{P}\exp\left(\frac{-l^3}{k_B T}\left(\frac{3}{2}P + \bar{P}\right)\right) \times \sum_{n=1}^{\infty}\frac{\bar{P}^n}{n!}\left(\frac{l^3}{k_B T}\right)^n \frac{(3P/2)^{3n/2}}{\Gamma(3n/2)}\left(\frac{l^3}{k_B T}\right)^{3n/2}$$

However, this is not the distribution of these quantities produced by the boundary condition algorithm. Analyzing the procedure for insertion and deletion of particles into a cell to maintain a given target pressure $\bar{P}$, one finds that the probability to have a number of particles n in the boundary cell $\rho_{bc}(n)$ is proportional to the probability of observing an instantaneous

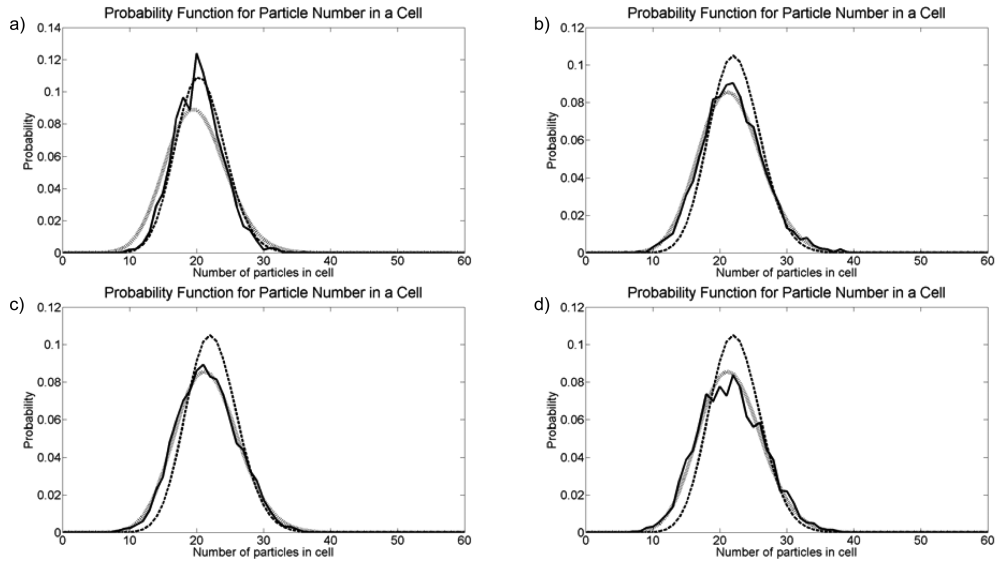

Figure 3. Plots of the particle number distribution for cells of differing depths into the channel for an equilibrium simulation with a pressure of 82.3 MPa. Within the *XY* plane, all of the cells are centered at (9.5,9.5). For panel (a), top left, the z value is 0.5 nm, for panel (b), top right, the z value is 9.5 nm, for panel (c), bottom left, the z value is 14.5 nm, and for panel (d), bottom right, the z value is 19.5 nm. The simulation data are shown as a solid line, eq 4 is shown as a dotted line, and eq 5 is shown as a dashed line. The temperature is 298 K in panel (a) and 275 K for panels (b)−(d). For panel (a), the data follow the distribution of eq 5. By panel (b), the data have adopted the profile of eq 4.

pressure equal to $\bar{P}$ in a cell containing n particles. Hence, the insertion and deletion algorithm generates a number distribution of

$$\rho_{bc}(n) = \frac{1}{\Gamma(3n/2)}\left(\frac{3l^3\bar{P}}{2k_BT}\right)^{3n/2} \times \left(\sum_{k=1}^{\infty}\frac{1}{\Gamma(3k/2)}\left(\frac{3l^3\bar{P}}{2k_BT}\right)^{3k/2}\right)^{-1}$$

in the inlet boundary cell. For typical values of the average number of particles in a cell of volume l^3, $\bar{n} = \bar{P}l^3/(k_BT)$, the probability density $\rho_{bc}(n)$ is slightly narrower than the equilibrium density $\rho_e(n)$, as is evident from the plots of the particle densities in Figure 3.

From similar considerations, one finds that the probability density of the pressure is significantly different and narrower in the boundary cell than it is in an equilibrium cell. It is also a discontinuous function and can be approximated as

$$p_{bc}(P) = \begin{cases} p_1(P) & P < \bar{P} \\ p_2(P) & P = \bar{P} \\ p_3(P) & \bar{P} < P \le 2\bar{P} \\ 0 & P > 2\bar{P} \end{cases} \qquad (5)$$

where

$$\begin{aligned} p_1(P) &= f_2(P)(f_1(P) - f_1(2(\bar{P} - P))) + f_3(P) \\ p_2(P) &= 2f_2(P) - 1/(2\bar{P}) \\ p_3(P) &= f_2(2\bar{P} - P)(f_1(P) - f_1(2(\bar{P} - P))) + f_3(2\bar{P} - P) \end{aligned}$$

and the functions f_1, f_2, and f_3 are

$$\begin{aligned} f_1(P) &= \mathrm{erf}\left(\sqrt{\frac{3l^3P}{2k_BT}}\right) - \sqrt{\frac{6l^3P}{\pi k_BT}}\exp(-3l^3P/(2k_BT)) \\ f_2(P) &= \frac{1}{2\bar{P}} + \frac{1}{2\bar{P}}\int_0^P \left[\frac{1}{P-\tilde{P}}\exp\left(\frac{3l^3(P-\tilde{P})}{2k_BT}\right) \times \right. \\ &\qquad \left. \sum_{n=1}^{\infty}\frac{1}{\Gamma(3n/2)}\left(\frac{3l^3(P-\tilde{P})}{2k_BT}\right)^{3n/2}\right] d\tilde{P} \\ f_3(P) &= \int_0^P \left(f_2(\tilde{P})\sqrt{\frac{2\bar{P}-P-\tilde{P}}{2\pi}}\left(\frac{3l^3}{k_BT}\right)^{3/2} \times \right. \\ &\qquad \left. \exp(-3l^3(2\bar{P} - P - \grave{P})/(2k_BT))\right) d\tilde{P} \end{aligned}$$

The narrow distribution of density and pressure in the inlet cells allows for stable control of the thermodynamic variables driving the flow through the channel. As the goal of these boundary conditions is to simulate flow in the section of the channel that is well removed from any changes in channel geometry or transient mechanical effects from a pump, it would be ideal if the boundary condition algorithms reproduced the equilibrium distributions when the head pressure is zero. However, the equilibrium distributions, particularly for the pressure, are too broad to maintain stable boundary conditions.

The number and pressure distributions for cells in layers z = 0.5, 9.5, 14.5, and 19.5 nm resulting for the boundary condition algorithm are shown in Figures 3 and 4. From these figures, it is clear that the simulations confirm the analytically predicted forms of these distributions. Note that the system has relaxed from the inlet distributions to the expected equilibrium distributions at a distance of 14.5 nm from the inlet cell. During this process, there is a decrease in the cell temperature and a corresponding increase in density (see Figure 8). For the simulations shown, the temperature drops from 298 to 275 K and the average cell density increases from roughly 20 to 21 particles. Because the influence of the narrow pressure distribution that results from the boundary conditions at the boundary cells does not persist far into the channel, their effect can be removed by adding additional layers of buffer cells or by restricting the cells in which thermodynamic properties are monitored to those in the interior of the channel.

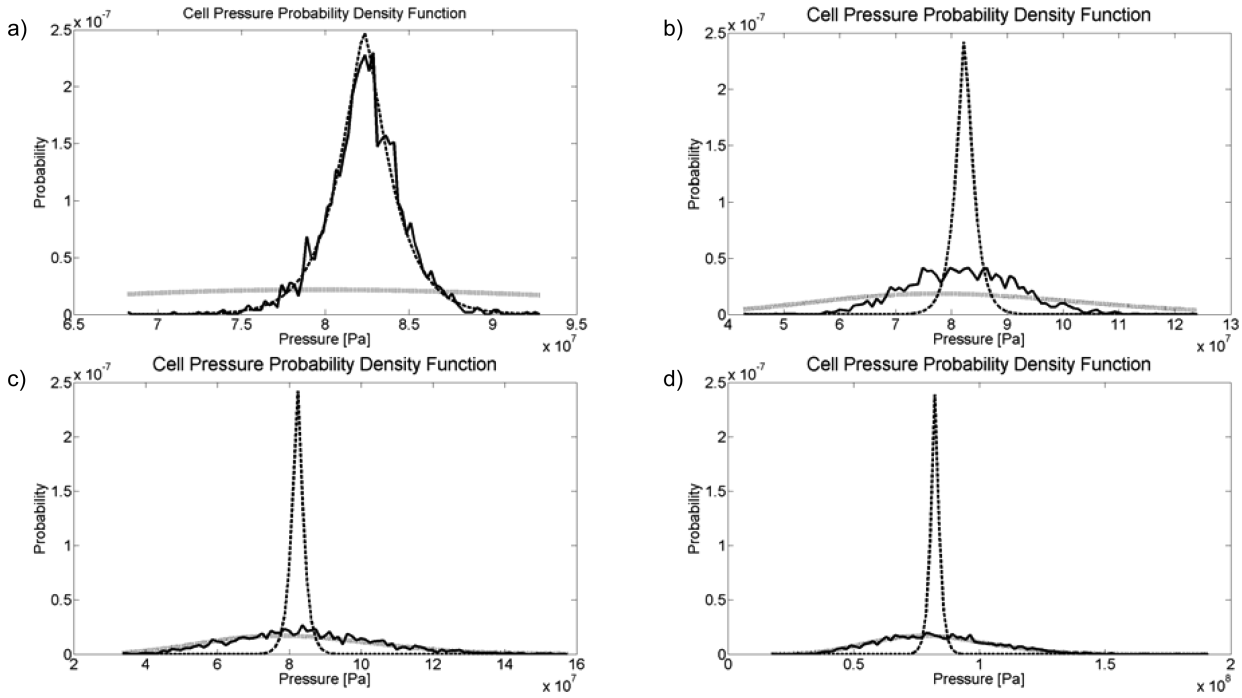

Figure 4. Plots of the pressure density function for cells of differing depths into the channel for the same cells and conditions as in Figure 3. For panel (a), top left, the z value is 0.5 nm, for panel (b), top right, the z value is 9.5 nm, for panel (c), bottom left, the z value is 14.5 nm, and for panel (d), bottom right, the z value is 19.5 nm. The simulation data are shown as a solid line, eq 4 is shown as a dotted line, and eq 5 is shown as a dashed line. For panel (a), the data follow the trend of eq 7. For panel (b), the data are intermediate between the two equations. In panel (c), the data have adopted the profile of eq 5.

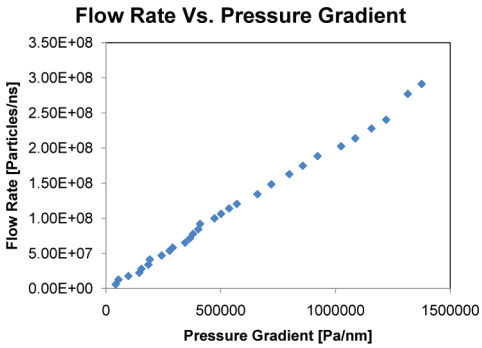

Figure 5. Plot of flow rate vs pressure gradient. The flow rate shows a linear dependence on the pressure gradient. This dependence has a slope of 208.2 ± 2.4 particles/ns/Pa and an intercept of $-2.8 \pm 1.0 \times 10^6$ particles/ns.

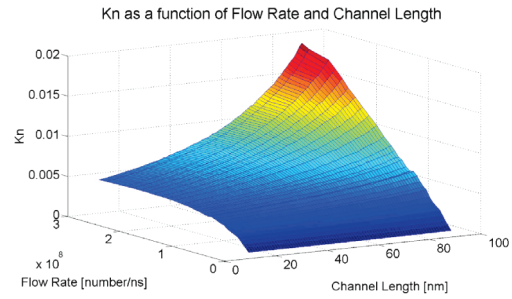

Figure 6. Plot of the Knudsen number across the length of the channel for various flow rates. K_n increases along both axes of the graph; however, there is a greater than linear increase across the length of the channel and a less than linear increase as the flow rate increases.

Flow Simulations

Under conditions of nonzero pressure gradient, the sink/source boundary conditions should establish a steady-state flow from the high-pressure inlet boundary cells to the low-pressure outlet cells. To verify that the correct flow profile was induced by a given pressure differential, a number of simulations with different pressure drops from inlet to outlet were carried out. From the equations in the Appendix, it is evident that the pressure and the Knudsen number, K_n, are expected to vary along the length of the channel, and the only constant measures across the channel in each simulation are the flow rate and the pressure gradient. Figure 5 illustrates the flow rate as a function of the pressure gradient, and Figure 6 illustrates K_n along the center of the channel ($x = y = 0$) as a function of the channel length. As the flow rate equations in the Appendix suggest, the flow rate in Figure 5 has a roughly linear dependence on the pressure gradient because the viscosity is roughly proportional to the pressure. As can be seen in Figure 6, K_n increases along the length of the channel. This is caused by the decrease in pressure along the length of the channel, which increases the mean free path length, and the increase in fluid velocity, which decreases the characteristic length of the system. As the flow rate increases, the velocity increases, which decreases the characteristic length. However, the local pressure is also higher, which decreases the mean free path length. Essentially, these are competing effects, with the increase in inlet pressure favoring a decrease in K_n, whereas the increase velocity increases the Knudsen number. Hence, even for the highest pressure gradient, the value of K_n is less than 0.01 in the inlet, well below the limit of around 0.1 where the NS equation ceases to be valid. The highest observed Reynolds number was 18.8 ± 0.3, which indicates that the flow field is laminar. Thus, the NS series solution without slip boundary conditions is an appropriate model for the inlet velocity distribution.

The pressure across the channel is shown as function of flow rate in Figure 7. As would be expected from the symmetry of the channel, the pressure is uniform across the channel cross section ($x-y$ plane). The regression values for the inlet and outlet pressure at $z = 10$ and 90 nm were used for calculation of the

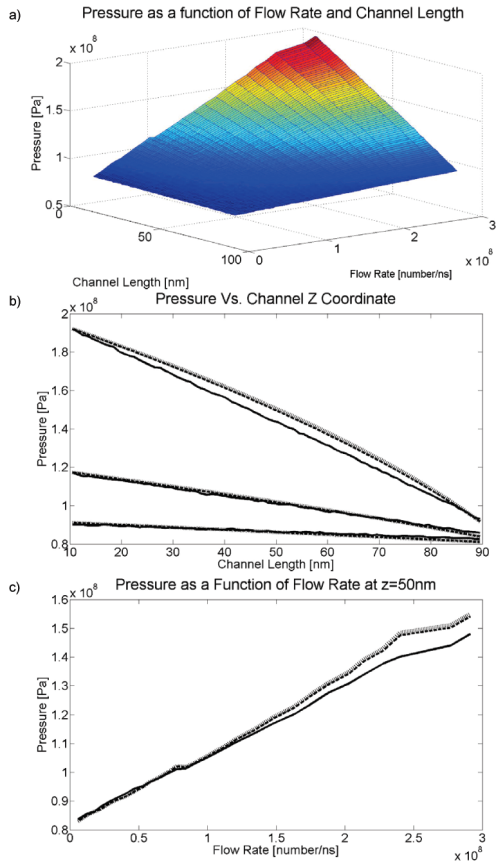

Figure 7. Pressure as a function of the flow rate and position across the length of the channel. The top graph, (a), shows the simulation data. The middle graph, (b), contrasts the pressure data with the results of the Navier−Stokes simulations along the length of the channel. The top set of lines is for a flow rate of $2.77 \pm 0.08 \times 10^8$ particles/ns, the middle set is for a flow rate of $7.78 \pm 0.26 \times 10^7$ particles/ns, and the bottom set is for a flow rate of $1.78 \pm 0.21 \times 10^7$ particles/ns. The bottom graph, (c), contrasts the pressure in the center of the channel, the point of maximum deviation, with the results of the Navier−Stokes simulations as a function of the flow rate. In panels (b) and (c), the simulation data are represented by a solid line, the NS solution with slip boundary conditions is represented by a dashed line, and the NS solution without slip boundary conditions is represented by a dotted line. The simulation data show a linear decrease in the pressure, whereas the simulations have an arced profile.

series solution profiles; hence there is a perfect agreement between the simulation data and NS solutions at those points. However, the simulations show a linear decrease in the pressure while the series solutions have a significant $\sqrt{z}$ component to the pressure profile, which causes a deviation between the theory and the results.

The solutions to the NS equation presented in the Appendix were obtained assuming an isothermal flow; however, the simulations applied an adiabatic boundary condition. For flow in a real channel, there will be a decrease in the temperature of the fluid due to its isentropic expansion;[21] hence, the simulations should possess a temperature drop even if though the Navier−Stokes solutions do not possess this feature. The temperature of the simulation as a function of the channel length and the flow rate is shown in Figure 8. Although the specification of the outlet temperature, which serves as a local thermostat, minimizes the temperature drop, there is still a decrease in temperature across the length of the channel. In the simulation with the highest flow rate, this decrease in temperature (from inlet to outlet) was 10 K. In addition to this decrease, there is a drop in the temperature in the channel relative to the

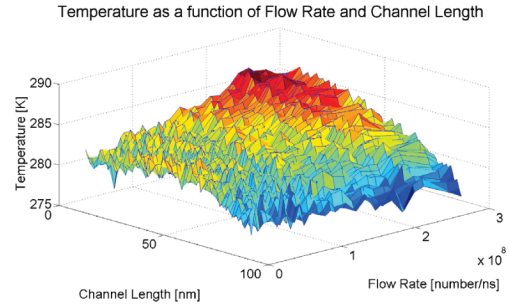

Figure 8. Temperature as a function of the flow rate and position across the length of the channel. The data show an increase in inlet temperature as the flow rate increases and a decrease in the temperature across the channel.

temperature specified in the boundary conditions. For the equilibrium system, it drops roughly 7%, whereas for the highest flow rate run, the temperature drops roughly 4%. This is likely due to the relaxation of the system to the steady-state pressure distribution from the very narrow pressure distribution enforced by the boundary condition algorithm. The strong flow field likely mitigates this effect at higher flow rates.

This decrease in temperature leads to an increase in the fluid density. The Navier−Stokes solutions and the simulation data are shown for the density and the velocity in Figures 9 and 10, respectively. At low flow rates of less than 7.6×10^7 particles/ns, the inlet density is lower than the NS solutions would predict. This may be attributed to some particle back flow that does not exist at high flow rates. At flow rates greater than 2.2×10^7 particles/ns, the $\sqrt{z}$ component in the NS pressure equations leads to an arc that results in a higher density. The velocity predicted by the simulations is consistent with the velocity predicted by the series solutions. The data follow the predictions of the slip solution to the Navier−Stokes equation. This is consistent with the boundary conditions used.

The slip at the center of a wall ($x = 10$, $y = 0$, $z = 50$) is plotted versus the flow rate in Figure 11. The estimates of the shear flow are consistent with the predicted values of the NS equation with diffusive slip boundary conditions but agree within error bars. The slip flow boundary condition in the solution was based on eq 2, which suggests that the slope of a plot of the slip velocity versus the product of the mean free path length and the shear rate at the wall should have a value of unity if the boundary conditions simulate diffusive collisions. This plot is shown in Figure 12 and shows a streamwise momentum accommodation of 0.96 with standard error of 0.04, which is in agreement with the theoretical value of 1.

The fluid velocity at the center of the channel is plotted along the x dimension ($y = 0$ nm, $z = 50$ nm) for various flow rates in Figure 13. For low flow rate simulations, there is too much noise in the data to indicate which Navier−Stokes solution agrees better with the simulation results. For the higher flow rate simulations, the results match the slip boundary condition profiles better than the nonslip conditions. The moderating effect of slip on the flow profile is also quite visible in the differences between the slip and nonslip solutions.

Conclusions

This article has presented a method to simulate gas flow in a channel with adiabatic diffusive boundary conditions using an MPC fluid. The flow field was created using a modified source−sink algorithm that specified inlet pressure, temperature, and velocity and outlet pressure and temperature. The inlet velocity distribution was calculated using a series solution of

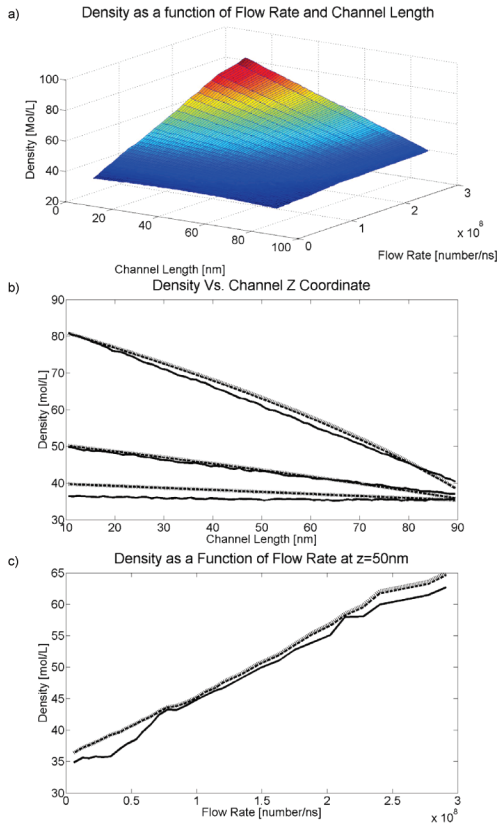

Figure 9. Density as a function of the flow rate and position across the length of the channel. The top graph, (a), shows the simulation data. The middle graph, (b), contrasts the density data with the results of the Navier−Stokes simulations along the length of the channel. The top set of lines is for a flow rate of $2.77 \pm 0.08 \times 10^8$ particles/ns, the middle set is for a flow rate of $7.78 \pm 0.26 \times 10^7$ particles/ns, and the bottom set is for a flow rate of $1.78 \pm 0.21 \times 10^7$ particles/ns. The bottom graph, (c), contrasts the density in the center of the channel with the results of the Navier−Stokes simulations as a function of the flow rate. In panels (b) and (c), the simulation data are represented by a solid line, the NS solution with slip boundary conditions is represented by a dashed line, and the NS solution without slip boundary conditions is represented by a dotted line. The density increases roughly linearly with the flow rate, though the simulation inlet density is lower than the NS solution density at low flow rates. The simulation data show a similar linear decrease in density across the channel along the channel, whereas the Navier stokes solutions have an arced profile that mirrors the pressure formula.

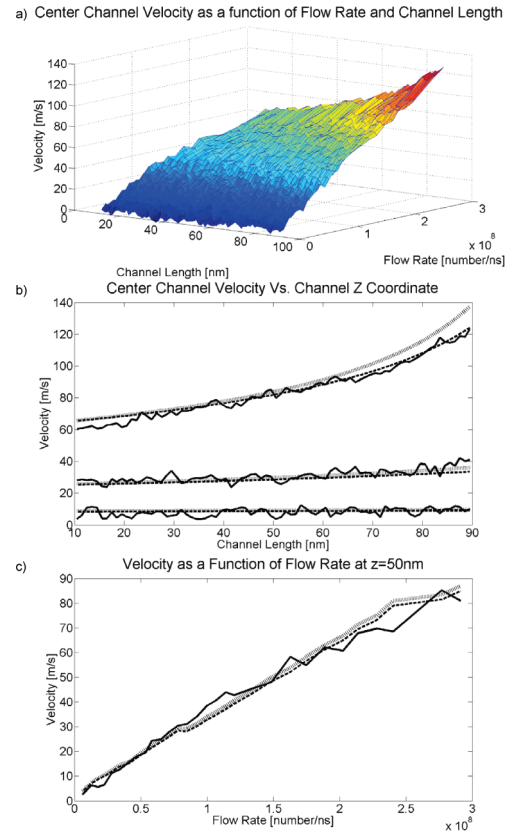

Figure 10. Center channel velocity as a function of the flow rate and position across the length of the channel. The top graph, (a), shows the simulation data. The middle graph, (b), contrasts the velocity data with the results of the Navier−Stokes simulations along the length of the channel. The top set of lines is for a flow rate of $2.77 \pm 0.08 \times 10^8$ particles/ns, the middle set is for a flow rate of $7.78 \pm 0.26 \times 10^7$ particles/ns, and the bottom set is for a flow rate of $1.78 \pm 0.21 \times 10^7$ particles/ns. The bottom graph, (c), contrasts the velocity at the end of the channel, $z = 90$, which is the point of maximum deviation, with the results of the Navier−Stokes simulations as a function of the flow rate. In panels (b) and (c), the simulation data are represented by a solid line, the NS solution with slip boundary conditions is represented by a dashed line, and the NS solution without slip boundary conditions is represented by a dotted line. Because of the noise in the data, it is difficult to identify which solution to the NS equation fits the simulation data better.

the Navier−Stokes equation without slip boundary conditions for the isothermal flow of an ideal gas. The boundary conditions are solely determined by the pressure, temperature, and physical dimensions of the channel.

The results of the simulations were compared to the results of the series solutions of the Navier−Stokes equation under the assumption of an isothermal flow. This comparison showed a close agreement between the simulation values and the Navier−Stokes solution with diffusive slip boundary conditions. The only deviations between these flow profiles appear to be due to the assumption that the fluid flow is isothermal. With adiabatic boundary conditions, the isentropic expansion of the fluid was partially converted to a temperature drop of the fluid along the channel length. Hence, the simulation density was higher and the velocity was lower than predicted from the Navier−Stokes equation. As the pressure gradient increased, so did the rarefaction and the deviation between the two analytical solutions and the simulations.

Despite the deviations observed in the velocity profile relative to the simulations at high flow rates, using the NS solution for

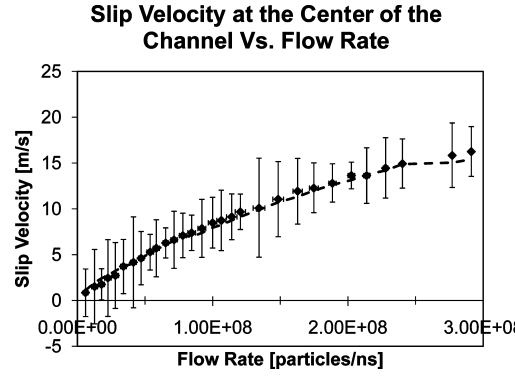

Figure 11. Slip velocity as a function of flow rate. The simulation data (markers) are consistent with the predictions of the slip data from the NS solution (dashed line).

the velocity profile at the first inlet cell is an efficient method of establishing boundary conditions for particle-based simulations of channel flow. The specification of the mean velocity in the first cell stabilizes the algorithm with respect to fluctuations

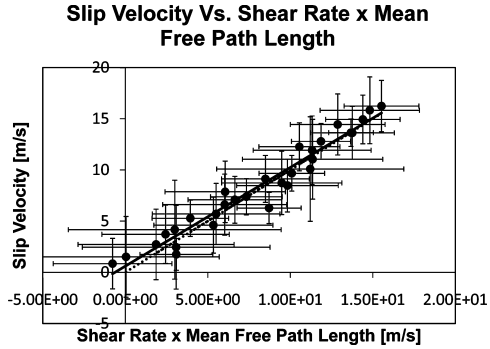

Figure 12. Slip velocity vs the product of shear rate and mean free path length. The slope of this line should be the streamwise momentum accommodation, which has a value of 1 for diffusive collisions. The data (solid line) have a slope of 0.96 ± 0.04 and an intercept of 0.6 ± 0.2, whereas the theory (dotted line) has a slope of 1 and an intercept of 0.

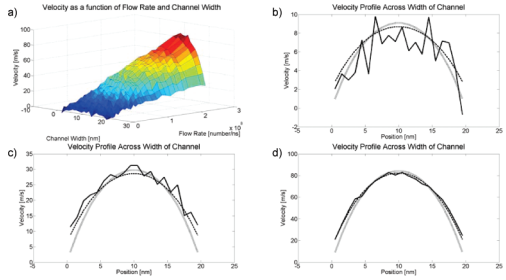

Figure 13. Velocity profile across the width of the channel ($y = 0$ nm, $z = 50$ nm) as a function of the flow rate. The top left graph, (a), shows the simulation data. The top right graph, (b), contrasts the velocity profile with the results of the Navier−Stokes solutions for a simulation with a flow rate of $1.78 \pm 0.21 \times 10^7$ particles/ns. The bottom left graph, (c), contrasts the velocity profile with the results of the Navier−Stokes solutions for a simulation with a flow rate of $7.78 \pm 0.26 \times 10^7$ particles/ns. The bottom right graph, (d), contrasts the velocity profile with the results of the Navier−Stokes solutions for a simulation with a flow rate of $2.77 \pm 0.08 \times 10^8$ particles/ns. In Figures (b)−(d), the simulation data are represented by a solid line, the NS solution with slip boundary conditions is represented by a dashed line, and the NS solution without slip boundary conditions is represented by a dotted line. The simulations clearly show slip at the boundary conditions with the walls. The simulation results are consistent with the results of the NS solution with slip boundary conditions.

in local cell velocities and particle number without introducing a significant bias that persists far into the channel.

Although the simulations presented here used an MPC algorithm, these solutions could be used to calculate boundary velocity profiles for hybrid DSMC or MD simulations. As these methods can simulate a more complex fluid, it would be worthwhile to investigate fluids with a nonideal equation of state and use the energy balance equation with a finite element method, though this would require considerable computational overhead relative to the series solution.

The MPC model presented here is of particular value for the purpose of investigating conformational changes of surface immobilized polymers under the effects of pressure-driven flow and shear or the effect of changes in channel morphology (e.g., a right angle bend or a weir) on the flow field itself. Such studies are underway. The strength of the MPC algorithm is its simplicity, which allows up to a microsecond of simulation of flow for channels of micrometer size containing millions of fluid particles, and makes it possible to study a small network of channels given modern computational resources. The ability of the modified source−sink algorithm to model large systems, as well as its reliance on parameters that can be determined with ease (pressure, temperature, and flow rate measurements), makes it ideal for feasibility studies and preliminary design of real-world devices.

Acknowledgment. This work was supported by a grant from the Natural Sciences and Engineering Research Council of Canada.

Appendix: Derivation of the Navier−Stokes Solution

In this appendix, the solution of the Navier−Stokes equation is outlined for isothermal fluid flow with and without slip boundary conditions in the square channel. This solution follows the method of Shah for an incompressible fluid[35] and is similar to the results of Arkillic et al.;[21] however, for a square channel, the simplifying assumption of a double parabola in the x and y dimensions cannot be made. The solution is used in the text to compare with simulation results as well as to provide a mean velocity in the first inlet cell. Results of the derivation for the pressure $P(z)$ as a function of the position z along the channel length, the component of the fluid velocity v_z along the length of the channel, as well as important numbers, such as the Knudsen number K_n and Reynolds number R_e, that characterize hydrodynamic flow, are summarized in Table 1.

The use of an isothermal boundary condition eliminates the need for an energy balance equation; hence, only the mass balance equations, momentum balance equation, and an equation of state are necessary to describe the dynamics of a fluid. For an MPC fluid without explicit interparticle interactions, the equation of state is that of an ideal gas. For a square channel of length L and height H, the mass balance equation for the MPC fluid is

$$Q = \int_{-H/2}^{H/2}\int_{-H/2}^{H/2} \rho(z)\bar{v}_z(x,y,z)\,dx\,dy = \frac{P(z)\bar{v}_z(z)H^2}{k_B T}$$

where Q is the constant z-independent flow rate, $\rho(z)$ is the fluid density, $\bar{v}_z(z)$ is the mean fluid velocity averaged over the channel cros section, and $P(z)$ is the local pressure. The momentum balance equation for flow in a square channel is

$$\frac{\partial \tau_{zx}}{\partial x} + \frac{\partial \tau_{zy}}{\partial y} + \frac{\partial P}{\partial z} = 0$$

where τ_{zx} is the shear stress acting in the z direction on the x-normal surface of the differential volume element. Inserting Newton's viscosity relation, $\tau_{zx} = \mu[(\partial v_z)/(\partial x)]$, where μ is the shear viscosity and v_z is the z component of the velocity vector, the momentum balance equation reduces to

$$\frac{\partial^2 v_z}{\partial x^2} + \frac{\partial^2 v_z}{\partial y^2} = -\frac{1}{\mu}\frac{\partial P}{\partial z} = C \qquad (6)$$

where C is a constant.

Because of symmetry constraints, the flow profile has to be even about the central axis of the channel in both the x and the y directions, and eq 6 can be solved using the cosine Fourier series

TABLE 1: Predicted Form for Isothermal Flow in a Square Channel of Width *H* and Length *L*[a]

$P(z)$	$-\alpha + \sqrt{\alpha^2 + \left(\frac{24\pi^5}{192 - \pi^5}\right)\frac{Qk_BT}{H^4}\mu z + P_{in}(P_{in} + 2\alpha)}$	slip
	$\sqrt{P_{in}^2 - \frac{56.9084k_BTQ}{H^4}\mu z}$	no-slip
$v_z(x, y, z)$	$P^0(z)\sum_{j=1}^{\infty}\frac{(-1)^{j-1}}{(2j-1)^3}\left(1 - \frac{\cosh(\Omega_j y)}{\cosh(\Omega_j H/2) + \Omega_j\lambda\lvert\sinh(\Omega_j H/2)\rvert}\right)\cos(\Omega_j x)$	slip
	$\frac{2\Delta P(z)H^2}{z\mu\pi^3}\left(1 + \frac{P_{in}}{P(z)}\right)\sum_{j=1}^{\infty}\frac{(-1)^{j-1}}{(2j-1)^3}\left(1 - \frac{\cosh(\Omega_j^0 y)}{\cosh((2j-1)\pi/2)}\right)\cos(\Omega_j^0 x)$	no-slip
Q	$\frac{H^3(P_{in} - P_{out})}{2\mu\pi^5 L}\left(\left(\frac{\pi^5 - 192}{12}\right)\frac{H(P_{out} + P_{in})}{k_BT} + \frac{\pi^5 - 256}{\sqrt{2}\pi r^2}\right)$	slip
	$\frac{(P_{in} - P_{out})(P_{in} + P_{out})H^4}{56.9084\mu k_BTL}$	no-slip
P_o	$\left(\frac{(H + 2\lambda)^3}{12H^3} - \frac{16(H + 2\lambda)^5}{\pi^5H^4(H + (2 + \pi)\lambda)}\right)^{-1}$	slip
	28.4542	no-slip
R_e	$\frac{H^2\Delta P(z)}{2\mu^2\pi^5 L}\left(\left(\frac{\pi^5 - 192}{12}\right)\frac{H(P(z) + P_{in})}{k_BT} + \frac{\pi^5 - 256}{\sqrt{2}\pi r^2}\right)$	slip
	$\frac{\Delta P(z)(P_{in} + P(z))H^3}{56.9084\mu^2 k_BTL}$	no-slip
K_n	$\frac{k_BTP_o}{2\sqrt{2}H\pi^6 r^2 zP(z)}\left(\frac{P_{in}}{P(z)} - 1\right)\left(\left(\frac{\pi^5 - 192}{12}\right)\left(1 + \frac{P_{in}}{P(z)}\right) + \frac{k_BT(\pi^5 - 256)}{\sqrt{2}\pi r^2 P(z)}\right)$	slip
	$\frac{k_BT\Delta P(z)(P(z) + P_{in})}{2\sqrt{2}\pi r^2 zP(z)^3}$	no-slip

[a] In this table, $\alpha = [(\pi^5 - 256)/(\pi^5 - 192)][(6k_BT)/(\sqrt{2}H\pi r^2)]$, $\Delta P(z) = P_{in} - P(z)$, $P^0(z) = [(2(H + 2\lambda)^2P_o)/(\pi^8 H)]\{[(P_{in})/(P(z))] - 1\}[(\pi^5 - 192)/(12\mu z)](2\alpha - H\Delta P(z))$, $\Omega_j = ((2j - 1)\pi)/(H + 2\lambda)$, and $\Omega_j^0 = ((2j - 1)\pi)/(H)$.

$$v_z(x, y, z) = \sum_{n=1,3,\ldots}^{\infty} a_n(y)\cos\left(\frac{n\pi x}{W}\right) \tag{7}$$

Under nonslip boundary conditions, where $v_z = 0$ at the channel walls, the width W of the channel is the physical width H. Substituting eq 7 into eq 6 yields

$$\sum_{n=1,3,\ldots}^{\infty}\left(\frac{\partial^2 a_n(y)}{\partial y^2} - \frac{n^2\pi^2}{W^2}a_n(y)\right)\cos\left(\frac{n\pi x}{W}\right) = C \tag{8}$$

which has the general solution of $a_n(y)$

$$a_n(y) = c_1\cosh\left(\frac{n\pi y}{W}\right) + c_2\sinh\left(\frac{n\pi y}{W}\right) - \frac{4CW^2}{n^3\pi^3}(-1)^{(n-1)/2}$$

where c_1 and c_2 are the constants of integration. Symmetry conditions imply that $c_2 = 0$, and c_1 is determined from the slip boundary conditions at the walls where $x = H/2$ or $y = H/2$

$$v_{slip} = \alpha\lambda\left.\frac{dv_z(x, y)}{dx}\right|_{x=H/2} = \alpha\lambda\left.\frac{dv_z(x, y)}{dy}\right|_{y=H/2} \tag{9}$$

where α is the streamwise momentum accommodation, which is 1 for diffusive boundary conditions.[21] Hence

$$a_n\left(\frac{H}{2}\right) = \lambda\left.\frac{da_n(y)}{dy}\right|_{y=H/2} \tag{10}$$

and c_1 can be determined to yield the following expression for eq 8

$$v_z(x, y, z) = -\frac{4W^2}{\mu\pi^3}\left(\frac{dP}{dz}\right)\sum_{j=1}^{\infty}\frac{(-1)^{j-1}}{(2j-1)^3}\cos(\Omega_j x)\times\left(1 - \frac{\cosh(\Omega_j y)}{\cosh(\Omega_j H/2) + \Omega_j\lambda\lvert\sinh(\Omega_j H/2)\rvert}\right) \tag{11}$$

where $\Omega_j = (2j - 1)\pi/W$.

Thus far, the effective width has not been specified for slip boundary conditions. W can be calculated by substituting eq 11 into eq 9. Inserting the definition of Ω_j, one finds that, to a good approximation

$$W\cot\left(\frac{\pi H}{2W}\right) = \pi\lambda$$

which implies that, for $W - H \ll W$, $W \approx H + 2\lambda$, and hence, $\Omega_j \approx (2j - 1)\pi/(H + 2\lambda)$.

Using eq 11, the average velocity is

$$\begin{aligned}\bar{v}_z(z) &= \int_{-H/2}^{H/2}\int_{-H/2}^{H/2} v_z(x,y,z)\,\mathrm{d}x\,\mathrm{d}y \\ &= -\frac{8W^3}{\mu\pi^4H^2}\left(\frac{\mathrm{d}P}{\mathrm{d}z}\right)\sum_{j=1}^{\infty}\frac{(-1)^{j-1}}{(2j-1)^4}\sin(\Omega_jH/2)\times \\ &\qquad \left(H + \left(\frac{2}{\Omega_j}\right)\frac{1}{\coth(\Omega_jH/2) + \Omega_j\lambda}\right)\end{aligned}$$

Using this equation, the Poiseuille number, a dimensionless measure of the body force defined as the proportionality constant between the pressure gradient and the average velocity, is given by

$$\begin{aligned}P_o &= -\frac{H^2}{\bar{v}\mu}\left(\frac{\mathrm{d}P}{\mathrm{d}z}\right) \\ &= -\frac{\pi^4H^4}{8W^3}\left(\sum_{j=1}^{\infty}\frac{(-1)^{j-1}}{(2j-1)^4}\sin(\Omega_jH/2)\times \right. \\ &\qquad \left.\left(H + \left(\frac{2}{\Omega_j}\right)\frac{1}{\coth(\Omega_jH/2) + \Omega_j\lambda}\right)^{-1}\right.\end{aligned}$$

Assuming that $H \gg 2\lambda$ and $\Omega_jH/2 \approx (2j - 1)\,\pi/2$, the transcendental functions can be eliminated to yield

$$P_o = -\frac{\pi^4H^4}{8W^3}\left(H\sum_{j=1}^{\infty}\frac{(-1)^{j-1}}{(2j-1)^4} - \frac{2W}{\pi}\sum_{j=1}^{\infty}\frac{1}{(2j-1)^5}\left(\frac{1}{1+\Omega_j\lambda}\right)\right)^{-1}$$

This first summation term can be computed exactly, $\sum_{j=1}^{\infty}(2j - 1)^{-4} = \pi^4/96$, while the second summation converges quickly and is well-approximated by its first term. Hence, to a good approximation, the Poiseuille number can be written as

$$P_o = \left(\frac{W^3}{12H^3} - \frac{16W^5}{\pi^5H^4(H + (2 + \pi)\lambda)}\right)^{-1} \qquad (12)$$

Inserting the definition of the Poiseuille number into the mass balance equation yields the differential equation

$$\bar{v}_z = -\frac{H^2}{P_o\mu}\left(\frac{\mathrm{d}P}{\mathrm{d}z}\right) = \frac{k_BTQ}{PH^2}$$

Substituting eq 12 into this equation and recalling the value of W, the flow rate can be written as

$$\frac{k_BTQ}{H^2} = \left(\frac{\mathrm{d}P}{\mathrm{d}z}\right)\left(\frac{16(H + 2\lambda)^5P}{\mu H^2\pi^5(H + (2 + \pi)\lambda)} - \frac{(H + 2\lambda)^3P}{12\mu H}\right)$$

Assuming that $H \gg \lambda$, this equation simplifies to

$$\frac{k_BTQ}{H^2} = \left(\frac{\mathrm{d}P}{\mathrm{d}z}\right)\left(\frac{16(H^2 + 8\lambda H)P}{\mu\pi^5} - \frac{(H^2 + 6\lambda H)P}{12\mu}\right)$$

Using $\lambda = k_BT/(2^{1/2}\pi r^2P)$ for the mean free path and solving the equation yields a quadratic expression for the local pressure

$$P(z)^2 + \left(\frac{256 - \pi^5}{192 - \pi^5}\right)\frac{12k_BTP(z)}{\sqrt{2}H\pi r^2} = \left(\frac{24\pi^5}{192 - \pi^5}\right)\frac{Qk_BT\mu z}{H^4} + P_{\mathrm{in}}^2 + \left(\frac{256 - \pi^5}{192 - \pi^5}\right)\frac{12k_BTP_{\mathrm{in}}}{\sqrt{2}H\pi r^2}$$

Rearranging this expression and evaluating $P(z)$ at the outlet, the flow rate can also be solved to yield

$$Q = \frac{H^3(P_{\mathrm{in}} - P_{\mathrm{out}})}{2\mu\pi^5L}\times\left(\left(\frac{\pi^5 - 192}{12}\right)\frac{H(P_{\mathrm{out}} + P_{\mathrm{in}})}{k_BT} + \frac{\pi^5 - 256}{\sqrt{2}\pi r^2}\right) \qquad (13)$$

and hence

$$\left(\frac{\mathrm{d}P}{\mathrm{d}z}\right) = \frac{P_o}{2H\pi^5z}\left(1 - \frac{P_{\mathrm{in}}}{P(z)}\right)\times \left(\left(\frac{\pi^5 - 192}{12}\right)H(P(z) + P_{\mathrm{in}}) + (\pi^5 - 256)\frac{k_BT}{\sqrt{2}\pi r^2}\right)$$

Putting this definition back into eq 11 yields the final expression for the velocity profile

$$\begin{aligned}v_z(x,y,z) = \frac{2W^2P_o}{\mu\pi^8Hz}\left(\frac{P_{\mathrm{in}}}{P(z)} - 1\right)\times\left(\left(\frac{\pi^5 - 192}{12}\right)H(P(z) - P_{\mathrm{in}}) + \right. \\ \left.(\pi^5 - 256)\frac{k_BT}{\sqrt{2}\pi r^2}\right)\sum_{j=1}^{\infty}\frac{(-1)^{j-1}}{(2j-1)^3}\cos(\Omega_jx)\times \\ \left(1 - \frac{\cosh(\Omega_jy)}{\cosh(\Omega_jH/2) + \Omega_j\lambda|\sinh(\Omega_jH/2)|}\right) \qquad (14)\end{aligned}$$

The Reynolds number, a measure of the relative importance of inertial to viscous forces in the fluid used to distinguish turbulent from laminar flow regimes, is given as

$$R_e = \frac{\rho\bar{v}_z(z)H}{\mu} = \frac{Q}{H\mu}$$

Inserting eq 13, the Reynolds number can be written as

$$R_e = \frac{H^2(P_{\mathrm{in}} - P(z))}{2\mu^2\pi^5L}\times\left(\left(\frac{\pi^5 - 192}{12}\right)\frac{H(P(z) + P_{\mathrm{in}})}{k_BT} + \frac{\pi^5 - 256}{\sqrt{2}\pi r^2}\right) \qquad (15)$$

The characteristic length for the system for the Knudsen number

$$\begin{aligned}D &= \rho\left(\frac{\partial\rho}{\partial z}\right)^{-1} \\ &= \frac{2\pi^5zHP(z)^2}{P_o(P_{\mathrm{in}} - P(z))}\left(\left(\frac{\pi^5 - 192}{12}\right)H(P(z) + P_{\mathrm{in}}) + \right. \\ &\qquad \left.\frac{k_BT(\pi^5 - 256)}{\sqrt{2}\pi r^2}\right)^{-1}\end{aligned}$$

Finally, the Knudsen number can be written as

$$K_n = \frac{k_B T P_o}{2\sqrt{2} H \pi^6 r^2 z P(z)} \left(\frac{P_{in}}{P(z)} - 1 \right) \times \left(\left(\frac{\pi^5 - 192}{12} \right) \left(1 + \frac{P_{in}}{P(z)} \right) + \frac{k_B T (\pi^5 - 256)}{\sqrt{2} \pi r^2 P(z)} \right) \quad (16)$$

The derivation of these results without slip boundary conditions follows directly by changing the boundary condition from eq 9 to $v_z(\pm H/2, y, z) = v_z(x, \pm H/2, z) = 0$.

References and Notes

(1) Chin, C. D.; Linder, V.; Sia, S. K. *Lab Chip* **2007**, *7*, 41–51.
(2) Kavassalis, P.; Oppenheim, I. *Physica* **1988**, *148A*, 521–555.
(3) Schofield, J.; Lim, R.; Oppenheim, I. *Physica A* **1992**, *181*, 89–135.
(4) Schofield, J.; Oppenheim, I. *Physica A* **1994**, *204*, 555–605.
(5) Bird, G. A. *Molecular Gas Dynamics and the Direct Simulation of Gas Flows*; Oxford University Press: New York, NY, 1994.
(6) Hoogerbrugge, P. J.; Koelman, J. M. V. A. *Europhys. Lett.* **1992**, *19*, 155–160.
(7) Malevanets, A.; Kapral, R. *J. Chem. Phys.* **1999**, *110*, 8605–8613.
(8) Peikos, E. S.; Breuer, K. S. *J. Fluids Eng.* **1996**, *118*, 464–469.
(9) Xue, H.; Fan, Q.; Shu, C. *Probab. Eng. Mech.* **2000**, *15*, 213–219.
(10) Wang, M.; Li, Z. *Int. J. Heat Mass Transfer* **2006**, *49*, 1696–1702.
(11) Steiner, T.; Cupelli, C.; Zengerle, R.; Santer, M. *Microfluid. Nanofluid.* **2009**, *7*, 307–323.
(12) Fedosov, D. A.; Karniadakis, G. E.; Caswell, B. *J. Chem. Phys.* **2008**, *128*, 144903.
(13) Allahyarov, E.; Gommper, G. *Phys. Rev. E* **2002**, *66*, 036702.
(14) Evans, D. J.; Morriss, G. P. *Comput. Phys. Rep.* **1984**, *1*, 297–343.
(15) Li, J.; Liao, D.; Yip, S. *Phys. Rev. E* **1998**, *57*, 7259–7267.
(16) Kapral, R. *Adv. Chem. Phys.* **2008**, *140*, 89–146.
(17) Ihle, T.; Kroll, D. M. *Phys. Rev. E* **2001**, *63*, 020201.
(18) McQuarrie, D. A. *Statistical Mechanics*; University Science Books: Sausalito, CA, 2000.
(19) Ihle, T.; Tüzel, E.; Kroll, D. *Europhys. Lett.* **2006**, *73*, 664.
(20) Tenenbaum, A.; Ciccotti, G.; Gallico, R. *Phys. Rev. A* **1982**, *25*, 2778–2787.
(21) Arkillic, E. B.; Schmidt, M. A.; Breuer, K. S. *J. Microelectromech. Syst.* **1997**, *6*, 167–178.
(22) Maxwell, J. C. *Philos. Trans. R. Soc. London* **1879**, *170*, 231–256.
(23) Renksizbulut, M.; Niazmand, H.; Tercan, G. *Int. J. Therm. Sci.* **2006**, *45*, 870–881.
(24) Jie, D.; Diao, Z.; Cheong, K. B.; Yong, L. K. *J. Micromech. Microeng.* **2000**, *10*, 372–379.
(25) Yu, Z. T. F.; Lee, Y.-K.; Wong, M.; Zohar, Y. *J. Microelectromech. Syst.* **2005**, *14*, 1386–1398.
(26) Zhang, W.; Zia, D. *Mol. Simul.* **2007**, *33*, 1223–1228.
(27) Damean, N.; Regtien, P. P. L. *Sens. Actuators, A* **2001**, *90*, 96–101.
(28) Weilin, Q.; Mohiuddin, G.; Dongqing, L. *Int. J. Heat Mass Transfer* **2000**, *43*, 353–364.
(29) Ihle, T.; Tüzel, E.; Kroll, D. *Phys. Rev. E* **2005**, *72*, 046707.
(30) Hecht, M.; Harting, J.; Ihle, T.; Herrmann, H. J. *Phys. Rev. E* **2005**, *72*, 011408.
(31) Tüzel, E.; Strauss, M.; Ihle, T.; Kroll, D. M. *Phys. Rev. E* **2003**, *68*, 036701.
(32) Nelder, J. A.; Mead, R. *Comput. J.* **1965**, *7*, 308–313.
(33) Straume, M.; Johnson, M. J. *Methods Enzymol.* **1992**, *210*, 117–129.
(34) VanderNoot, T. J.; Abrahams, I. *J. Electroanal. Chem.* **1998**, *448*, 17–23.
(35) Shah, R. K.; London, A. L. *Laminar Flow and Forced Convection in Ducts: A Source Book for Compact Heat Exchanger Analytical Data*; Academic Press: New York, NY, 1978.

JP1055914